

# **TITLE**

Carmela Filosa

Cover art:  
Photography:

A catalogue record is available from the Eindhoven University of Technology Library

ISBN: 978-90-386-3972-7

Copyright © 2017 by C. Filosa.

All rights are reserved. No part of this publication may be reproduced, stored in a retrieval system, or transmitted, in any form or by any means, electronic, mechanical, photocopying, recording or otherwise, without prior permission of the author.

**title**

**PROEFSCHRIFT**

ter verkrijging van de graad van doctor aan de  
Technische Universiteit Eindhoven, op gezag van de  
rector magnificus prof.dr.ir. F.P.T. Baaijens, voor een  
commissie aangewezen door het College voor  
Promoties, in het openbaar te verdedigen

door

Carmela Filosa

geboren te Torre del greco, Italië

Dit proefschrift is goedgekeurd door de promotoren en de samenstelling van de promotiecommissie is als volgt:

voorzitter: prof.dr.

1<sup>e</sup> promotor: prof.dr. W.L. IJzerman

copromotor: dr. J.H.M. ten Thije Boonkkamp

leden:

Het onderzoek of ontwerp dat in dit proefschrift wordt beschreven is uitgevoerd in overeenstemming met de TU/e Gedragscode Wetenschapsbeoefening.

“ ”



# Abstract

**Keywords:**



# Contents

<b>1</b>	<b>Introduction</b>	<b>1</b>
1.1	Motivation . . . . .	1
1.2	Methods and results . . . . .	1
1.3	Content of this thesis . . . . .	1
<b>2</b>	<b>Non imaging optics</b>	<b>3</b>
2.1	Radiometric and photometric variables . . . . .	3
2.2	Reflection and refraction law . . . . .	3
2.3	Fresnel reflection . . . . .	3
<b>3</b>	<b>Ray tracing</b>	<b>5</b>
3.1	Ray tracing for two-dimensional optical systems . . . . .	5
3.2	Monte Carlo ray tracing . . . . .	5
3.3	The phase space method for a TIR-collimator . . . . .	5
3.4	Numerical results and discussion . . . . .	15
<b>4</b>	<b>Ray tracing on phase space</b>	<b>19</b>
4.1	Phase space concept . . . . .	19
4.2	The edge-ray principle . . . . .	19
4.3	The PS method . . . . .	19
<b>5</b>	<b>Two different approaches to compute the boundaries in target phase space</b>	<b>21</b>
5.1	The $\alpha$ -shapes approach . . . . .	21
5.2	The two-faceted cup . . . . .	24
5.3	Results for a TIR collimator . . . . .	24
5.4	The triangulation refinement approach . . . . .	24
5.5	The two-faceted cup . . . . .	24
5.6	Results for a Parabolic reflector . . . . .	24
5.7	Results for the Compound Parabolic Concentrator . . . . .	24
5.8	Results for a TIR collimator . . . . .	24

<b>6 The inverse ray mapping method: analytic approach</b>	<b>25</b>
6.1 Explanation of the method . . . . .	25
6.2 Results for the two-faceted cup . . . . .	25
6.3 Results for the multi-faceted cup . . . . .	25
6.4 Discussions . . . . .	25
<b>7 The extended ray mapping method</b>	<b>27</b>
7.1 Explanation of the method . . . . .	27
7.2 Bisection procedure . . . . .	27
7.3 Results for a parabolic reflector . . . . .	27
7.4 Results for two different kind of TIR-collimators . . . . .	27
<b>8 Extended method to systems with Fresnel reflection</b>	<b>29</b>
<b>9 Conclusions and remarks</b>	<b>31</b>
<b>Summary</b>	<b>33</b>
<b>Curriculum Vitae</b>	<b>35</b>
<b>Acknowledgments</b>	<b>37</b>
<b>Bibliography</b>	<b>39</b>

# **Chapter 1**

# **Introduction**

Do some changes

- 1.1 Motivation**
- 1.2 Methods and results**
- 1.3 Content of this thesis**



## **Chapter 2**

# **Non imaging optics**

- 2.1 Radiometric and photometric variables**
- 2.2 Reflection and refraction law**
- 2.3 Fresnel reflection**



# Chapter 3

## Ray tracing

### 3.1 Ray tracing for two-dimensional optical systems

### 3.2 Monte Carlo ray tracing

### 3.3 The phase space method for a TIR-collimator

sec:method

Ray tracing uses single rays to describe the propagation of light through an optical system. The influence of diffraction on the transport of a ray is neglected and geometrical modeling of an optical system is considered. In this work only Snell's law is taken into account and Fresnel reflection is not considered. Generally, the method can be implemented for two or more dimensions and for any optical system. We focus on the example of a TIR-collimator in two-dimensions. First, we introduce the classical ray tracing method and we specify the geometry of the optical system used in our model; second, we describe the phase space procedure.

#### 3.3.1 Classical ray tracing and geometry of the optical system

The ray tracing process consists of tracing each ray, which is considered to be a broken line, through a non-imaging system. In the following, the two-dimensional procedure is explained. Given a Cartesian coordinate system  $(x, z)$ , a two-dimensional optical system is defined. To obtain the photometric variables at the target, the propagation of light from the source  $\mathcal{S}$  to the target  $\mathcal{T}$  is computed. In this work, we calculate the output intensity for the TIR-collimator, the profile of which is depicted in Figure 3.1.

The TIR-collimator we analyze is an optical system rotationally symmetric with respect to the  $z$ -axis and consists of a lens (line 2), two broken lines adjacent to the lens (formed by the collection of the segments 3, 4, and 5 and 9, 10 and 11), two curved lines (labeled with 6 and 8) and the top formed by a horizontal segment (line 7). The lens and the broken lines are refractive lines while, the curved lines are designed in such a way that light is internally reflected (which explains the name TIR). The light source  $\mathcal{S}$  (line 1) and the target  $\mathcal{T}$  (line 12) are two straight segments normal to the optical axis and are located in air ( $n_1 = 1$ ) while the volume inside the collimator is

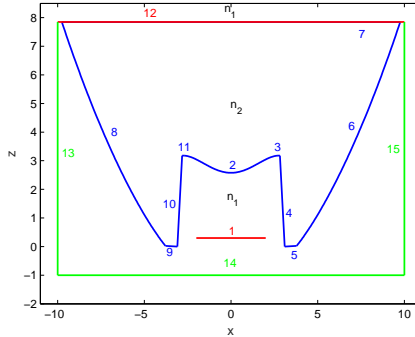


Figure 3.1: Shape of the TIR-collimator. Each line of the system is labeled with a number. The source  $\mathcal{S} = [-2, 2]$  (line number 1) is located at an height  $z_s = 0.3$  from the  $x$ -axis. The target  $\mathcal{T} = [-9.7, 9.7]$  (line 12) is parallel to the source and is located at an height  $z_t = 7.85$ . The shape of the collimator is shown as a blue line. Three detectors depicted with green lines (lines 13, 14, and 15) are located at the left, the right and the bottom of the optical system.  $n_1 = 1$  is the refraction index of the medium (air) where the source and the target are located, and  $n_2 = 1.5$  the refraction index of the medium (glass) inside the optical system. The sagitta of the lens is equal to 0.6.

filled with a material with index of refraction  $n_2 = 1.5$  (e.g. glass). The collimator is surrounded by two vertical and two horizontal lines (lines 13, 15, 12 and 14, respectively) that receive the light exiting from the optical system; among these, the horizontal one at the top is assumed to be the light target and, it is located at a small distance from the top.

From now on, the coordinates  $(x_i, z_i)_{(i=1, \dots, 15)}$  denote the intersection of the rays with the line  $i$  and,  $\mathbf{s}_i = (-\sin t_i, \cos t_i)$  is the direction vector of the rays that leave the line  $i$ , where  $t_i \in (-\pi/2, \pi/2)$  is the angle that the ray forms with the  $z$ -axis, measured counterclockwise. Therefore, a ray segment between  $(x_i, z_i)$  and  $(x_{i+1}, z_{i+1})$  is parameterized by:

$$\mathbf{r}(s) = \begin{pmatrix} x_i - s \sin(t_i) \\ z_i + s \cos(t_i) \end{pmatrix} \quad s \geq 0, \quad (3.3.1) \quad [\text{parametrization}]$$

where  $s$  denotes the arc-length.

A Lambertian optical source is considered; hence, the intensity over an interval  $J = [-a, a]$  emitted in the direction  $t$  is given by:

$$I(t) = I_0 \cos(t), \quad (3.3.2) \quad [\text{lambertian source}]$$

where  $I_0 = 2aL$ ,  $L$  is the luminance, and  $t$  is the angle that the ray forms with respect to the optical axis, measured counterclockwise. As a result, in the case where  $L = 1$ ,  $I_0$  coincides with the source length; from Equation (3.3.2), the intensity at the source is deduced.

To compute the target intensity, we need to know how the optical system changes the direction of the rays during their propagation from the source to the target. To do this, we employ the ray tracing technique which can be summarized as follows: first, a ray from the source with initial position given by the coordinates  $(x_1, z_1)$  and

initial angle  $t_1$  with respect to the  $z$ - axis is traced and, the ray parametrization is implemented according to Equation (3.3.1). Second, the intersection point  $(x_i, z_i)$  between the ray and the line  $i$  that it hits first is computed. Third, the normal to the line hit at the point  $(x_i, z_i)$  is calculated to compute the change of direction of the ray. For the last step, the laws of reflection and refraction are implemented. The direction of the refractive ray is given by:

$$\mathbf{t} = n_{1,2} \mathbf{i} + \left[ \sqrt{1 - n_{1,2}^2 + n_{1,2}^2(\mathbf{n}, \mathbf{i})^2} - n_{1,2}(\mathbf{n}, \mathbf{i}) \right] \mathbf{n}, \quad (3.3.3) \quad \text{refract}$$

where  $n_{1,2} = n_1/n_2$  with  $n_1$  and  $n_2$  the refraction indexes of air and of glass, respectively. The unit vectors  $\mathbf{i}$  and  $\mathbf{t}$  describe the directions of the incident and refracted ray, respectively;  $\mathbf{n}$  is the normal to the line; it is also a unit vector and it is directed towards the interior of the optical system. Note that the positive sign before the square root is due to the convention to take the inward direction of the normal  $\mathbf{n}$  (see [3], chapter 4, p. 95-106, and, [?], chapter 12 p. 403-409). In the case where  $n_1 = -n_2$ , Equation (3.3.3) can be rewritten as the law of reflection:

$$\mathbf{t} = \mathbf{i} - 2(\mathbf{i}, \mathbf{n})\mathbf{n}. \quad (3.3.4) \quad \text{reflect}$$

Equation (3.3.4) is used when the total internal reflection condition holds, that is when the following inequality is true:

$$1 - n_{1,2}^2 + (\mathbf{n}, \mathbf{i})^2 < 0. \quad (3.3.5) \quad \text{eq: TIR}$$

For the TIR-collimator the previous condition occurs for the curved lines (lines 6 and 8 in Figure 3.1). Finally, the new parametrization of the ray is described by:

$$\mathbf{r}(s) = \begin{pmatrix} x_i + s t_x \\ z_i + s t_z \end{pmatrix}, \quad (3.3.6)$$

where  $t_x$  and  $t_z$  are the  $x$  and  $z$ -components of the new ray direction and are calculated from Equations (3.3.3) or (3.3.4). The points  $(x_i, z_i)$  and the new direction  $\mathbf{t}$  are computed until the ray hits the target and the previous procedure is repeated for each ray traced.

To obtain a reasonable approximation of the target intensity, a large number of rays has to be traced; the more rays are traced, the more accurate the target intensity is. Moreover, for the TIR-collimator shown in Figure 3.1, we do not have an explicit equation to describe the reflectors. Only the positions of a discrete set of points located on their curves are known. Therefore, we use spline interpolation to obtain a good approximation of the curved lines. In addition, to calculate the intersection points between the rays and these lines, the Newton-Raphson procedure is employed. Due to all these reasons, the ray-tracing method is a very slow procedure.

A frequently used ray tracing method in non-imaging optics is MC ray tracing [7] in which the rays are emitted from a random location and at random angle. They are traced through the system until they reach the target receiver. To calculate the output intensity, the target screen is divided into bins and the frequency of the rays that arrive at each bin is considered. The intensity restricted to a certain bin is obtained by dividing the number of rays that fall into that bin by the total number of rays traced. Although MC ray tracing is highly robust and does not require difficult

calculations, it has two main disadvantages. First, some information is lost because the flux of a ray is averaged over a bin. Second, some parts of the target are reached by a very small fraction of rays and, consequently, the intensity is unreliable in those parts. As a consequence, a large number of rays needs to be traced to obtain an accurate intensity making the MC method computationally expensive.

We provide a new method that employs the phase space representation of the optical system to avoid tracing rays where the luminance does not present any discontinuities. Phase space ray tracing is explained in the next section.

### 3.3.2 Phase space representation of the source and the target

In phase space each ray is described by its intersection point with the line it hits and the sine of the angle it forms with respect to the optical axis multiplied by the refractive index (see [?] chapter 2.1-2.3, [?], and [?] chapter 1 for details). In the following, the phase space is considered only for the source  $\mathcal{S}$  and the target  $\mathcal{T}$  and for no other line of the optical system. The rays in a two-dimensional system correspond to points with coordinates  $(x, \tau)$  and  $(q, \eta)$  in  $\mathcal{S}$  and  $\mathcal{T}$  phase space, respectively. We have indicated the ray positions with  $x$  and  $q$ , the angles formed with the normal with  $t$  and  $\theta$ , the refractive indexes with  $n_s$  and  $n_t$ , for  $\mathcal{S}$  and  $\mathcal{T}$ , respectively and, with  $\tau = n_s \sin(t)$  and  $\eta = n_t \sin(\theta)$  the directions of the rays.

The rays are represented by a unique point in phase space, both for  $\mathcal{S}$  and  $\mathcal{T}$ . More formally, the optical phase space for the light source is defined as:

$$\mathcal{P}_s = \mathcal{S} \times [-n_s, n_s]. \quad (3.3.7)$$

The target phase space is defined as

$$\mathcal{P}_t = \mathcal{T} \times [-n_t, n_t]. \quad (3.3.8)$$

The map  $\mathcal{M} : \mathcal{P}_s \rightarrow \mathcal{P}_t$  which describes how the optical system changes the rays is defined as:

$$\mathcal{M}(x, \tau) = (q, \eta). \quad (3.3.9)$$

For most optical systems, there is no way to determine an explicit expression for the map  $\mathcal{M}$  defined above. The idea is to apply the edge-ray principle [5] to a given set of rays at the source. The principle states that to map one region from the source to the target phase space it is sufficient to map the boundaries of those regions. Therefore, the boundaries of the source are mapped to the boundaries of the target and the regions where the luminance is different from zero are calculated. The intensity in target phase space is defined as a function of the output luminance:

$$I_{PS}(\eta) = \int_{\mathcal{T}_\eta} L_t(q, \eta) dq, \quad (3.3.10)$$

where, for a given constant  $\eta_0 \in [-1, 1]$ , the set  $\mathcal{T}_{\eta_0} = \{(q, \eta) \in \mathcal{T} \mid \eta = \eta_0\}$  and  $L_t(q, \eta)$  indicates the luminance at the target. As we use the target phase space to compute the output intensity, it is convenient to define it as a function of  $\sin(\theta)$  instead of  $\theta$ . Note that the luminance is positive in the entire  $\mathcal{P}_s$ , but not all parts of  $\mathcal{P}_t$  receive light emitted by the source. As a result,  $L_t$  has jump discontinuities where

it changes from zero to positive values. To understand where these discontinuities occur, further information about the rays is required. Because of this, for PS ray tracing not only the initial positions and the initial angles of the rays are stored, but also the optical lines they hit when they propagate through the system. A ray path  $\Pi$  is defined as the collection of lines hit by the ray. Rays that are close to each other at the source and leave the source at close angles follow the same path and hit the target at close positions and under close angles. All the rays that follow the same path are grouped together into the same subset of phase space. From now on, we indicate with  $p$  the number of all the possible paths  $(\Pi_j)_{j=1,\dots,p}$  encountered by the rays and, with  $R_{s,\Pi_j}$  and  $R_{t,\Pi_j}$  the regions corresponding to the rays that follow the path  $\Pi_j$  for the source and the target, respectively. The map  $\mathcal{M}$  defined in Equation (3.3.9) relates the regions  $R_{s,\Pi_j}$  to the regions  $R_{t,\Pi_j}$  for every  $j \in \{1, \dots, p\}$ . The edge-ray principle guarantees that the boundaries  $\partial R_{s,\Pi_j}$  and  $\partial R_{t,\Pi_j}$  are connected by the same map  $\mathcal{M}$ . Given two different paths  $\Pi_1$  and  $\Pi_2$ , the regions  $R_{t,\Pi_1}$  and  $R_{t,\Pi_2}$  do not overlap; they can have at most a common boundary. As a result, the discontinuities of the luminance occur exactly at the boundaries  $(\partial R_{t,\Pi_j})_{j=1,\dots,p}$ . Finally, the luminance at the target satisfies the following relations:

$$\begin{aligned} L_t(q, \eta) &> 0 & \text{for } (q, \eta) \in (R_{t,\Pi_j})_{j=1,\dots,p}, \\ L_t(q, \eta) &= 0 & \text{otherwise.} \end{aligned} \quad (3.3.11)$$

luminance

In addition, the luminance is conserved along a ray, so it remains constant inside every region  $(R_{t,\Pi_j})_{j=1,\dots,p}$ , (see [?], chapter 16). The output intensity is obtained from Equation (3.3.10). Therefore, the problem to compute the target intensity can be interpreted as the calculation of the boundaries  $(\partial R_{t,\Pi_j})_{j=1,\dots,p}$ . To this end, we define a triangulation on source phase space in such a way that more rays close to the boundaries are traced. The details of these procedures are explained in the next section.

### 3.3.3 Triangulation refinement of source phase space

The regions  $(R_{t,\Pi_j})_{j=1,\dots,p}$  can be defined only when some rays are traced. Given an initial set of rays, the rays closest to the boundaries  $(\partial R_{t,\Pi_j})_{j=1,\dots,p}$  are selected and more rays in their vicinity are created to get progressively better estimates of the boundaries. A more detailed description is provided below. A triangulation in  $\mathcal{P}_s$  is defined and a ray from every vertex  $(x_k, \tau_k)$  of the triangle is traced. The procedure starts tracing four rays with coordinates  $(x_k, \tau_k)_{k=1,\dots,4}$  that are located exactly at the corners of  $\mathcal{P}_s$  and, for each of them, the paths  $(\Pi_j)_{j=1,\dots,4}$ , are stored. Next, for some  $j \in \{1, \dots, 4\}$ , the grid is divided into two equal triangles joining two opposite vertices. For each triangle the rays located at its corners are traced. If the paths corresponding to those rays are different, one or more boundaries  $(\partial R_{t,\Pi_j})_{j=1,\dots,4}$  are expected to cross the triangle. In that case, the middle points  $(x_k, \tau_k)_{k=5,6,7}$  of each side of the triangle are added and three more rays with coordinates  $(x_k, \tau_k)_{k=5,6,7}$  are traced. Each refinement step leads to four new triangles (see Figure 3.2).

When all the rays in the corners of each triangle have the same path, it is not necessary to refine the triangles anymore. Note that it can happen that a region formed by rays that follow a path  $\Pi_j$  is located completely inside a triangle whose vertices are related to the same path  $\Pi_i$  with  $j \neq i$ . In that case the algorithm is not

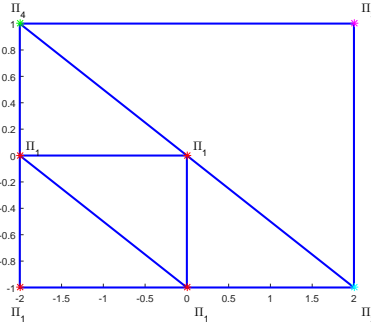


Figure 3.2: Triangulation refinement: when the rays related to the vertices of the triangles follow a different path a new refinement step is required. Each refinement step leads to four new triangles. The parameters values are  $\epsilon_{x_{max}} = 2$ ,  $\epsilon_{\tau_{max}} = 1$ ,  $\epsilon_{x_{min}} = 4$  and  $\epsilon_{\tau_{min}} = 2$ .

inement

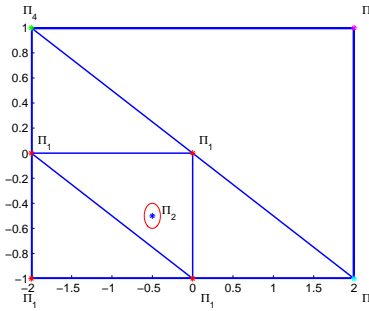


Figure 3.3: The red line encloses a region of rays that follow the path  $\Pi_2$  and is completely located inside a triangle. The algorithm is not able to detect that region and, a further refinement is required. The parameters values are  $\epsilon_{x_{max}} = 2$ ,  $\epsilon_{\tau_{max}} = 1$ ,  $\epsilon_{x_{min}} = 4$  and  $\epsilon_{\tau_{min}} = 2$ .

inside

able to detect that region, see Figure 3.3. To avoid this, two parameters  $\epsilon_{x_{min}}$  and  $\epsilon_{\tau_{min}}$  are defined for the  $x$ -axis and the  $\tau$ -axis, respectively. When the length of the sides of the triangle are greater than these parameters, a new triangle is defined even if its vertices correspond to the same path. Furthermore, two other parameters  $\epsilon_{x_{max}}$  and  $\epsilon_{\tau_{max}}$  are introduced to define a stopping criterion. The algorithm stops when the length of the sides of the triangles is smaller than  $\epsilon_{x_{max}}$  and  $\epsilon_{\tau_{max}}$ . The values of the parameters  $\epsilon_{x_{max}}$ ,  $\epsilon_{\tau_{max}}$ ,  $\epsilon_{x_{min}}$  and  $\epsilon_{\tau_{min}}$  determine the number of rays traced. Indeed, on the one hand,  $\epsilon_{x_{max}}$  and  $\epsilon_{\tau_{max}}$  can be decreased to obtain more rays close to the boundaries; on the other hand, a large number of rays in the interior of the regions can be traced decreasing the values of  $\epsilon_{x_{min}}$  and  $\epsilon_{\tau_{min}}$ .

Using the above procedure, rays increasingly closer to the boundaries are traced. For our optical system, the width of the  $x$ -axis in source phase space is two times the width of the  $\tau$ -axis. Thus, our choice is  $\epsilon_{\tau_{min}} = \frac{1}{2}\epsilon_{x_{min}}$  and  $\epsilon_{\tau_{max}} = \frac{1}{2}\epsilon_{x_{max}}$ . Figure 3.4 shows an example of a triangulation refinement of the source phase space with  $\epsilon_{x_{max}} = 0.1$  and  $\epsilon_{x_{min}} = 1$ . The triangulation refinement provides more triangles close to the boundaries  $\partial R_{s,\Pi_j}$  than those inside the regions  $R_{s,\Pi_j}$ .

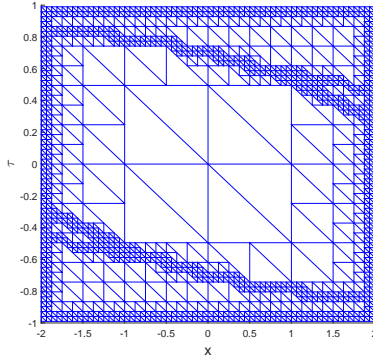


Figure 3.4: Triangulation refinement of source phase space: near the boundaries more rays are traced. The values of the parameters are  $\epsilon_{x_{max}} = 0.1$  and  $\epsilon_{x_{min}} = 1$ .

The paths  $(\Pi_j)_{j=1,\dots,p}$  followed by the rays located at the corner of the triangles are computed during the procedure and, the regions  $R_{s,\Pi_j}$  and  $R_{t,\Pi_j}$  are defined for each  $\Pi_j$ . Next, a criterion to select the values of the parameters  $\epsilon_{x_{min}}$  and  $\epsilon_{x_{max}}$  and a method to compute the boundaries  $\partial R_{t,\Pi_j}$  is provided. Furthermore, the output photometric variables are computed, the details are explained in the next section.

### 3.3.4 Photometric variables at the target

As mentioned in Section 3.3.3.2, the boundaries  $(\partial R_{t,\Pi_j})_{j=1,\dots,p}$  have to be calculated to compute the photometric variables at the target. Our method is based on the triangulation refinement of the source phase space. More rays close to the boundaries can be traced selecting increasingly smaller values for the parameters  $\epsilon_{x_{max}}$  and  $\epsilon_{\tau_{max}}$ . Once the algorithm stops, only the triangles that are expected to be crossed by a boundary are taken into account. By construction, each of these triangles has two vertices that follow the same path and one vertex that follows another path. The triangles are ordered in such a way that two of them are neighbors if they have a side in common. Given a path  $\Pi_j$  with  $j \in \{1, \dots, p\}$  the boundary  $\partial R_{s,\Pi_j}$  of the region corresponding to  $\Pi_j$  is approximated by those vertices of the triangles corresponding to the path  $\Pi_j$ . The boundaries  $\partial R_{t,\Pi_j}$  at the target are given by  $\mathcal{M}(\partial R_{s,\Pi_j})$  for every  $j \in \{1, \dots, p\}$ . To establish the minimum value of the parameter  $\epsilon_{x_{max}}$  that gives a good approximation of the boundaries  $\partial R_{t,\Pi_j}$ , a technique that exploits the conservation of the étendue in phase space is provided, (see [?], chapter 16). The essence of our approach is as follows.

We consider the étendue for the whole  $\mathcal{P}_s$  which is given by:

$$E_s = 2n_s a \sin(t_{max}), \quad (3.3.12)$$

where  $a$  is the length of the source and  $t_{max}$  is the maximum value of the angle that the rays make with the  $z$ -axis. The étendue of a set of rays is defined by the area they occupy in phase space. For the TIR-collimator we considered (Figure 3.1), the area

of  $\mathcal{P}_s$  is equal to 7.92, as  $a = 4$  and  $\sin(t_{max}) = 0.99$ . The rays traced are uniformly distributed over  $\mathcal{P}_s$ , and they cover it entirely.

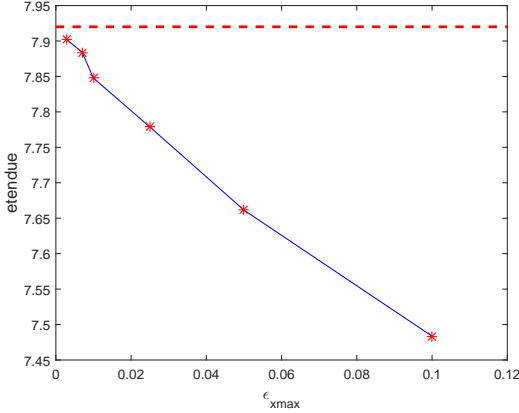


Figure 3.5: The total étendue as an area in PS is depicted with the dotted red line. The approximated étendue is computed for a range of values of  $\epsilon_{x_{max}}$ . Decreasing the value of the parameter the  $\epsilon_{x_{max}}$ , the étendue increases and reaches a good approximation of the exact étendue for  $\epsilon_{x_{max}} = 3 \cdot 10^{-3}$ .

éndueTS

The total étendue at the target  $E_t$  is given by the sum of the étendues related to each region  $R_{t,\Pi_j}$ :

$$E_t = \sum_{j=1}^p E(R_{t,\Pi_j}), \quad (3.3.13) \quad \text{eq:etenduetar}$$

where  $E(R_{t,\Pi_j})$  is the contribution to the étendue at the target given by the rays inside the region  $R_{t,\Pi_j}$ . Note that  $E_t$  is computed by also considering the area of the regions formed by the rays that hit the left and the right detectors (lines 13 and 14 in Figure 3.1).  $E(R_{t,\Pi_j})$  is defined by:

$$E(R_{t,\Pi_j}) = \iint_{R_{t,\Pi_j}} dq d\eta. \quad (3.3.14) \quad \text{etenduepartia}$$

To calculate the previous integral the triangulation refinement method is applied to the regions  $R_{s,\Pi_j}$  for a range of values of  $\epsilon_{x_{max}}$ , with an approximation of the boundaries  $\partial R_{s,\Pi_j}$  obtained for each of them. Therefore, the boundaries  $\partial R_{t,\Pi_j}$  are also computed and the intersection points  $(q_{\Pi_j,i}(\eta))_{i=1,\dots,r}$  between  $\partial R_{t,\Pi_j}$  and the horizontal line  $\eta = const$  are calculated for each  $j \in \{1, \dots, p\}$ , with  $\eta \in [-1, 1]$ . Ordering the points  $(q_{\Pi_j,i}(\eta))_{i=1,\dots,r}$  in ascending order, Equation (3.3.14) becomes:

$$E(R_{t,\Pi_j}) = \sum_{i=1}^m \int_{-1}^1 (q_{\Pi_j,2i}(\eta) - q_{\Pi_j,2i-1}(\eta)) d\eta, \quad (3.3.15) \quad \text{eq:etenduetar}$$

where  $m$  is the integer part of  $r/2$  and  $r$  is the number of the intersection points between  $\partial R_{t,\Pi_j}$  and the horizontal lines  $\eta = const$ . The integral in Equation (3.3.15)

is calculated by discretizing the interval  $[-1, 1]$  into  $Nb = 100$  sub-intervals of equal width and using the trapezoidal rule. Figure 3.5 shows that decreasing the value of the parameter  $\epsilon_{x_{max}}$  increases the values of the étendue at the target  $E_t$ , which reaches 7.9 when  $\epsilon_{x_{max}} = 0.3 \cdot 10^{-3}$ . We decide to stop the phase space refinement procedure when a good approximation of the étendue is obtained. Moreover, a criterion to establish the values of  $\epsilon_{x_{min}}$  is provided. For each value of  $\epsilon_{x_{max}}$  the étendue for a range of values of  $\epsilon_{x_{min}}$  is computed. As the computation of the boundaries does not depend on the number of rays inside the regions, the étendue remains constant when the value of  $\epsilon_{x_{min}}$  changes. We choose  $\epsilon_{x_{min}}$  as large as possible avoiding to trace rays that do not significantly contribute to the computation of the photometric variables at the target. The value of  $\epsilon_{x_{min}}$  depends on the distribution of the rays in phase space. For our optical system the parameter  $\epsilon_{x_{min}} = 1$ . Figure 3.6 and 3.7 show the approximation of the boundaries obtained for a set of  $6.9 \cdot 10^4$  rays. Five different paths are found and rays that follow the same path are depicted with the same color. Figure 3.6 shows that, choosing the values of the parameters as explained above, the regions  $R_{s,\Pi_j}$  almost completely cover the source phase space. As a consequence, the dark areas in Figure 3.7 correspond to parts of target phase space that are not reached by any ray that leaves the source and propagates through the meridional plane of the optical system. Note that, using the triangulation procedure explained in the previous section, more rays close to the boundaries are traced.

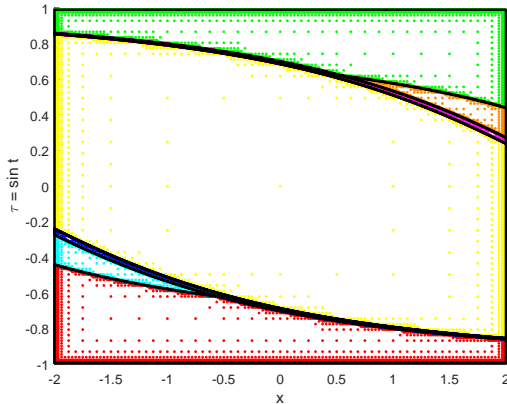


Figure 3.6: Distribution of the rays on source phase space. Around  $6.9 \cdot 10^4$  rays are traced using the triangulation refinement with parameters:  $\epsilon_{x_{min}} = 1$ ,  $\epsilon_{\tau_{min}} = 0.5$ ,  $\epsilon_{x_{max}} = 3 \cdot 10^{-3}$ ,  $\epsilon_{\tau_{max}} = 1.5 \cdot 10^{-3}$ . Rays that belong to the same region are depicted with the same color. The yellow rays follow the path  $\Pi_1 = (1, 2, 7, 12)$ ; the red rays follow the path  $\Pi_2 = (1, 10, 8, 7, 12)$ ; the green rays follow the path  $\Pi_3 = (1, 4, 6, 7, 12)$ ; the blue rays follow the path  $\Pi_4 = (1, 11, 7, 12)$ ; the magenta rays follow the path  $\Pi_5 = (1, 3, 7, 12)$ , the cyan rays hit the left detector (line 13) and follow the path  $\Pi_6 = (1, 10, 7, 8, 13)$  and, the orange rays hit the right detector (line 15) and follow the path  $\Pi_7 = (1, 4, 7, 6, 15)$ . Each number corresponds to a line of the TIR-collimator as shown in Figure 3.1. The boundaries are depicted with the black lines.

To conclude, we compute the target intensity which is defined in  $\mathcal{P}_t$  by Equation

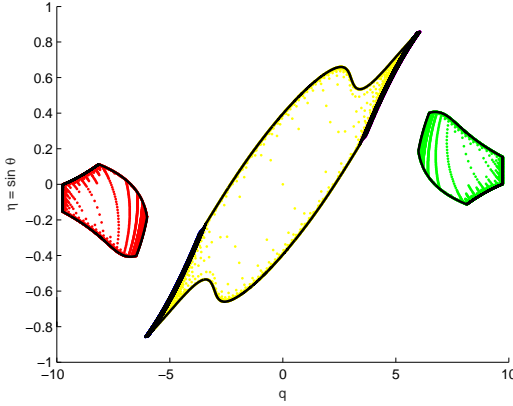


Figure 3.7: Target phase space representation of a set of  $6.9 \cdot 10^4$  rays. Only the rays that hit the target (line 12) are considered. The values of the parameters  $\epsilon_{x_{min}}, \epsilon_{x_{max}}, \epsilon_{\tau_{min}}, \epsilon_{\tau_{max}}$  and the choice of the colors for each path are the same as in Figure 3.6. The boundaries  $(\partial R_{t,\Pi_j})_{j=1,\dots,p}$  are computed through the triangulation method. The dark areas correspond to areas that are not hit by any meridional plane.

(3.3.10). From Equation (3.3.11), we obtain:

$$I_{PS}(\eta) = \sum_{i,j} \int_{q_{\Pi_j,2i-1}(\eta)}^{q_{\Pi_j,2i}(\eta)} L_t(q, \eta) dq, \quad (3.3.16) \quad \boxed{\text{eq: Ips}}$$

where the summation for the indices  $i$  is over all  $i = 1, 2, \dots, m$ , and the summation for the  $j$  indices is over all  $j$  for which the intersection between  $\eta = const$  and  $R_{t,\Pi_j}$  is not empty. The intensity is expressed as a function of the angular parameter  $\eta = n_t \sin(\theta)$ . In the case of a Lambertian source with  $L_s(x, \tau) = 1$ , the following relation for the intensity at the target holds:

$$I_{PS}(\eta) = \sum_{i,j} (q_{\Pi_j,2i}(\eta) - q_{\Pi_j,2i-1}(\eta)), \quad (3.3.17) \quad \boxed{\text{intensity_eta}}$$

where the relation  $n_t = 1$  and conservation of luminance along a ray are exploited, (see [?], chapter 16). We again notice that Equation (3.3.16) and (3.3.17) are valid when only two intersection points are found. If  $r > 2$  intersection points occur the sum of the distances  $(q_{2i} - q_{2i-1})_{i=1,\dots,m}$  needs to be computed. To calculate the intensity for all the possible directions, a uniform partitioning  $P : -1 \leq \eta_0 < \eta_1 \dots < \eta_{Nb} \leq 1$  of the interval  $J = [-1, 1]$  is considered, where  $Nb = 100$ . Eventually, the intensity for each  $\eta_h$ , with  $h = 0, 1, \dots, Nb$ , is obtained using relation (3.3.17). We compare the new method with the already existing MC ray tracing to show its efficiency.

The intensity for MC ray tracing is computed as follows. The partitioning  $P$  of  $J = [-1, 1]$ , used for the target phase space, is considered and the number of rays that fall into each bin  $([\eta_h, \eta_{h+1}])_{h=0,\dots,Nb-1}$  is calculated for all  $h \in \{0, \dots, Nb-1\}$ .

The intensity in the direction  $\eta_k \in [\eta_h, \eta_{h+1}]$  is approximated by:

$$\hat{I}_{MC}(\eta_k) = \frac{Nr([\eta_h, \eta_{h+1}])}{Nr([-1, 1])}, \quad (3.3.18)$$

for every  $(\eta_k = \frac{1}{2}(\eta_{h+1} + \eta_h))_{k=1,2,\dots,Nb}$ , where we have indicated the number of rays that fall into the bin  $[\eta_h, \eta_{h+1}]$  with  $Nr([\eta_h, \eta_{h+1}])$  and the total number of rays with  $Nr([-1, 1])$ . As  $\hat{I}_{MC}$  is normalized, a normalization of  $I_{PS}$  is also required to compare the two intensities. This normalization is calculated dividing the intensity by the étendue  $E_{\mathcal{T}}$  at the target:

$$\hat{I}_{PS}(\eta_k) = \frac{1}{E_{\mathcal{T}}} \int_{\eta_h}^{\eta_{h+1}} I_{PS}(\eta) d\eta \quad \text{for } k = 1, 2, \dots, Nb, \quad (3.3.19)$$

where  $E_{\mathcal{T}}$  is obtained by removing the étendue corresponding to the regions formed by the rays that hit the left and the right detectors from the total étendue  $E_t$ , computed in Equation (3.3.13) and shown in Figure 3.5. Note that the intensities are vectors of length  $Nb$ , and  $\hat{I}_{PS}(\eta_k)_{k=1,2,\dots,Nb}$  represent the intensities along the directions  $(\eta_k)_{k=1,\dots,Nb}$ . The accuracy of the intensity also depends on the number of bins considered in the partitioning  $P$ . Choosing  $Nb = 100$  results in a smooth profile of the intensity; hence, we decide to fix that value of  $Nb$ . The photometric variables at the target are now determined for MC and PS method. The numerical results are shown in the next section.

### 3.4 Numerical results and discussion

In this section a comparison between the MC and PS methods is presented. The MC and PS intensities are calculated several times increasing the number of rays  $Nr$  to improve the accuracy. Both approximate intensities are compared with an intensity taken as a reference. For some optical systems, there is an explicit solution for the target intensity but this is not the case for the TIR-collimator. Therefore, the reference intensity  $\hat{I}_{ref}$  is obtained considering  $1,7 \cdot 10^8$  rays in the MC simulation. We show how the error, defined as:

$$\text{error} = \frac{\sum_{h=1}^{Nb} |\hat{I}_{PS}(\eta_h) - \hat{I}_{ref}(\eta_h)|}{Nb}, \quad (3.4.1) \quad \boxed{\text{error}}$$

decreases with the increase in the number of rays. Table 3.1 describes how the number of rays traced affects the error estimation and shows the correlation between étendue and the number of rays, which is determined by the values of  $\epsilon_{x_{min}}$ ,  $\epsilon_{\tau_{min}}$ ,  $\epsilon_{x_{max}}$  and  $\epsilon_{\tau_{max}}$  as explained in Section 3.3.3.3. Next, the intensity  $\hat{I}_{MC}$  for the MC method is computed. Replacing  $\hat{I}_{PS}$  with  $\hat{I}_{MC}$  in Equation (3.4.1), the error between the reference intensity and the MC intensity is calculated. Increasing the number of rays traced in MC ray tracing, the error gradually decreases. In Table 3.2 the numerical results are reported.

The results listed in Table 3.1 and Table 3.2 are shown in Figure 3.8, where the red line depicts the behavior of the error for the PS intensity, and the blue line indicates the error for the MC simulation.

b





Table 3.1: Error values of the PS intensity

Number of rays	$\epsilon_{x_{max}}$	$\epsilon_{\tau_{max}}$	étendue	error
1 403	$1.0 \cdot 10^{-1}$	$5.00 \cdot 10^{-2}$	7.4836	$3.57 \cdot 10^{-4}$
3 237	$5.0 \cdot 10^{-2}$	$2.50 \cdot 10^{-2}$	7.6614	$2.22 \cdot 10^{-4}$
7 299	$2.5 \cdot 10^{-2}$	$1.25 \cdot 10^{-2}$	7.7787	$1.38 \cdot 10^{-4}$
15 919	$1.0 \cdot 10^{-2}$	$5.00 \cdot 10^{-3}$	7.8475	$7.31 \cdot 10^{-5}$
33 651	$7.0 \cdot 10^{-3}$	$3.50 \cdot 10^{-3}$	7.8839	$3.80 \cdot 10^{-5}$
69 330	$3.0 \cdot 10^{-3}$	$1.50 \cdot 10^{-3}$	7.9017	$2.02 \cdot 10^{-5}$

b





Table 3.2: Error values of the MC intensity

Number of rays	error <sub>MC</sub>
970	$2.20 \cdot 10^{-3}$
9 702	$6.60 \cdot 10^{-4}$
97 104	$1.74 \cdot 10^{-4}$
971 436	$6.34 \cdot 10^{-5}$
9 715 391	$2.06 \cdot 10^{-5}$

:table2

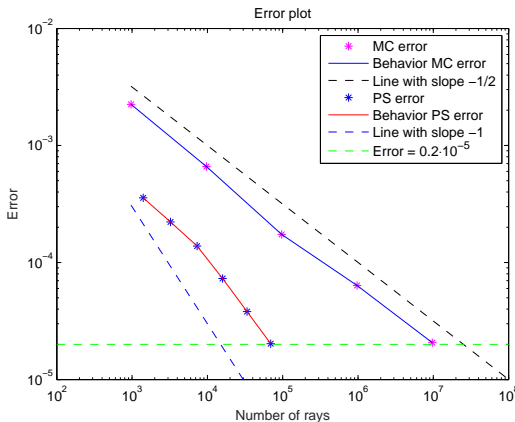


Figure 3.8: The red line depicts the error between the intensity on phase space and the reference intensity. The blue line shows the error between the Monte Carlo intensity and the reference intensity. The dashed black line represents a straight line with the slope equal to  $-\frac{1}{2}$ . The dashed blue line represents a straight line with the slope equal to  $-1$ . The horizontal dotted line shows that an error equal to  $2.00 \cdot 10^{-5}$  can be obtained tracing at least  $10^2$  times fewer rays in phase space.

Figure 3.8 shows that an error equal to  $2.00 \cdot 10^{-5}$  is obtained by tracing around  $9.7 \cdot 10^6$  rays for MC and only around  $6.9 \cdot 10^4$  in PS. The error decreases as  $\frac{1}{\sqrt{N_r}}$  for the MC method and as  $\frac{1}{N_r}$  for the PS simulation.

The intensity profile  $\hat{I}_{PS}(\eta)$  obtained with the phase space method and tracing around  $6.9 \cdot 10^4$  rays is depicted in Fig. 3.9 with a red line.  $\hat{I}_{PS}$  is hardly distinguishable from  $\hat{I}_{ref}$  (dashed blue line in Figure 3.9). The intensities are expressed as

g:error

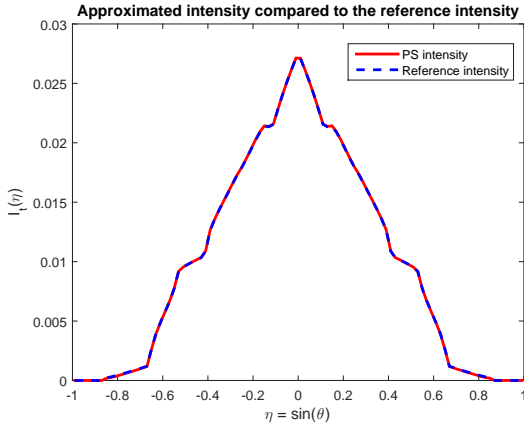


Figure 3.9: The red line shows the PS intensity at the target of the TIR-collimator. The reference intensity is depicted with the dotted blue line. The approximate intensity can hardly be distinguished from the exact intensity. The curves are functions of the angular parameter  $\eta = n_t \sin(\theta)$ .

**fig:intensityMCPS**

functions of  $\eta$  and thus, the curves in Figure 3.9 do not depict the spatial intensities.

Finally, we claim that PS ray tracing is also more accurate than the ray tracing procedure proposed by Moore (2013), [?]. The novelty of our approach compared to the method used by Moore, is briefly explained below. First, to compute the output intensity, we employ the phase space of the target. This avoids the use of any interpolation to compute the photometric variables and therefore, more accurate results are obtained. Second, in [?] all rays that leave the source start at the same position and only a sampling angular range is given. In our approach a rectangular source is considered thus, both the angular and spatial coordinates of each ray change. This extra variable can produce very irregular shapes of the regions at target phase space. To overcome this issue, we employ the edge-ray principle and we consider the regions at source phase space where the distribution of the rays is much more regular and the corresponding boundaries are easily computed. As a consequence, our procedure is suitable to compute the output intensity as function of both the angular or the spatial coordinates. Third, using the conservation of étendue, we provided a criterion to stop the triangulation refinement. In this way we can estimate the number of rays required to obtain the desired accuracy and thus, we avoid tracing more rays than necessary.



## Chapter 4

# Ray tracing on phase space

4.1 Phase space concept

4.2 The edge-ray principle

4.3 The PS method



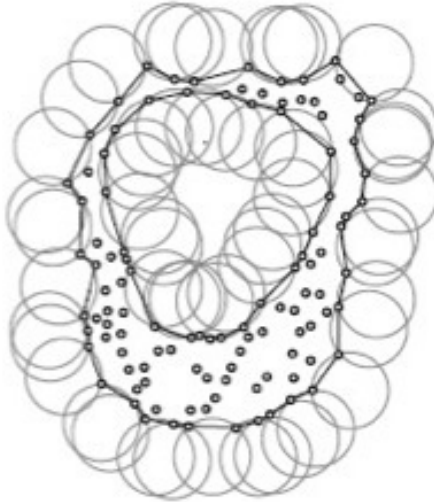
# Chapter 5

## Two different approaches to compute the boundaries in target phase space

### 5.1 The $\alpha$ -shapes approach

Given a finite set  $\mathcal{S}$  of points we want to determine the shape formed by these points.  $\alpha$ -shapes are geometrical objects which give us a good approximation of the shape of a given point set  $\mathcal{S}$ . Before giving a formal definition we explain an intuitive interpretation of  $\alpha$ -shapes. As mentioned in [1] we can think of an  $\alpha$ -shape as a mass of ice-cream with several chocolate pieces. The mass making up the space  $\mathbb{R}^3$  and the chocolate pieces are the point set  $\mathcal{S}$ . Then the aim is to find the shape formed by the chocolate pieces. We can use a spoon with a spherical shape and carve out all parts of the ice-cream without removing the chocolate pieces. We will obtain a shape formed by arcs and points (see figure below for the two-dimensional case). Straightening the arcs to triangles and line segments we have an intuitive description of what is called the  $\alpha$ -shape of  $\mathcal{S}$ . In our example, the parameter  $\alpha$  determines of the radius of the carving spoon. If  $\alpha$  is equal to 0 the shape degenerates to the point set  $\mathcal{S}$ . On the other hand, when  $\alpha \rightarrow \infty$  the  $\alpha$ -shape is simple the convex hull. More precisely the process is summarized as follows. Given a point cloud  $\mathcal{S}$  we start with a triangulation of it (a possible choice could be the Delaunay triangulation described in the next section). For each triangle we calculate the radius of the circumcircle. If the radius is larger than  $\alpha$  the triangle is removed from the shape. The rule of the parameter  $\alpha$  is highly significant in this procedure. Hence we have to choose it in such a way to get a better approximation. The choice of the parameter  $\alpha$  is closely related to the radius of the circumcircles. A possible strategy is to find the radius of the greater empty circumcircle. Thus  $\alpha$  is related to the density of the points. In particular we have:

$$\alpha = C \frac{1}{\Delta} , \quad (5.1.1)$$



g : shape

 Figure 5.1: Construction of  $\alpha$ -shape given a set of points in  $\mathbb{R}^2$ .

with  $C$  a constant that can be determined by a simulation and  $\Delta$  the density of the point set  $\mathcal{S}$  defined as:

$$\Delta = \frac{N}{\text{surface area}} , \quad (5.1.2)$$

where  $N$  is the number of points in  $\mathcal{S}$  and the surface area is the area inside the boundaries of the region formed by the points cloud. Hence  $\Delta$  is a constant. As mentioned above to find the  $\alpha$ -shape of a point cloud we need a triangulation and a possible choice could be the Delaunay triangulation. As explained in [4] we can see a Delaunay triangulation as the dual of a Voronoi diagram. Let us define a Voronoi diagram in a metric space.

**Definition 5.1.1.** Let  $X$  be a space endowed with a distance  $d$  and  $\mathcal{S} = \{S_1, \dots, S_n\}$  a set formed by subsets of  $X$ . The Voronoi cell  $R_k$  associated with the set  $S_k$  where  $k \in \{1, \dots, n\}$  is defined as follows:

$$R_k = \{\mathbf{x} \in X \mid d(\mathbf{x}, S_k) \leq d(\mathbf{x}, S_j) \quad \forall j \neq k\} , \quad (5.1.3)$$

where  $d(x, A) = \inf\{d(x, a) \mid a \in A\}$ . The Voronoi diagram is defined as the tuple of the cells  $(R_k)_{k \in \{1, \dots, n\}}$  that are assumed to be disjoint.

The simplest case that we can have is the two-dimensional case that is the case where  $X = \mathbb{R}^2$ . The tuple  $\mathcal{S} = \{1, \dots, n\} \subset \mathbb{R}^2$  is now a set of points. The Voronoi diagram of  $\mathcal{S}$  is a subsection of  $\mathbb{R}^2$  such that every other region around a point  $p \in \mathcal{S}$  contains all points that are closer to  $p$  than to every point in  $\mathcal{S}$ . A triangulation of the point set  $\mathcal{S}$  is a set of edges  $\mathcal{E}$  whose extremes are points of  $\mathcal{S}$  such that the faces of each triangle are bounded by three edges and any edge that is not in  $\mathcal{E}$  intersects one

of the existing edges. The Delaunay triangulation is the dual graph of the Voronoi diagram: it consists of vertices (the points in  $\mathcal{S}$ ) and it has an edge between two vertices if the two corresponding faces share an edge.

The Delaunay triangulation triangulates the convex hull of the point set  $\mathcal{S}$ . Instead, the  $\alpha$ -shape of a point set is formed only by the triangles (taken from the Delaunay triangulation) that satisfy the " $\alpha$ -test" and therefore is a suitable method to reconstruct the surface formed by a point cloud. Even if  $\alpha$ -shapes are a powerful tool to reconstruct surfaces, some simulations show that there exist surfaces that are not described well by  $\alpha$ -shapes. Indeed for some particular surface there exist no value of  $\alpha$  that includes all desired triangles and deletes all undesired triangles. For instance, since the parameter  $\alpha$  depends on the density of the point cloud, is intuitively clear that using  $\alpha$ -shapes for a non-uniform points set we won't get a good approximation of the surface. Furthermore, the  $\alpha$ -shape method doesn't work well when there is a sharp turn or a joint. In this case  $\alpha$ -shapes often give a "webbed-foot" appearance at such joints since they improperly connect the adjacent surfaces. Hence a generalization of "classical"  $\alpha$ -shapes is required. In the next section a method to solve the "density problem" for two separated and close objects is described. In [6] Teichmann and Capps present "Density-scaled  $\alpha$ -shapes". The first step of this method is to make a triangulation of the point cloud. Then the key idea is to compute somehow the point-density of each point and use this to get an approximation of the point density of a triangle. In this way one can reduce the  $\alpha$ -value in areas where the triangle's point density (see equation 5.1.6 for the definition) is higher than average in such a way that is possible to obtain a finer level of detail for areas that have an higher density. More precisely, each point  $\mathbf{p} \in \mathcal{S}$  has a local point density defined as

$$\delta(\mathbf{p}) = \sum_{\mathbf{q} \in \mathcal{S}} \left(1 - \frac{d(q, p)}{\lambda}\right) \quad \forall \mathbf{q} \text{ such that } d(\mathbf{p}, \mathbf{q}) < \lambda, \quad (5.1.4)$$

where  $\lambda$  is the constant radius of the local neighborhood and  $d(\mathbf{x}, \mathbf{y})$  is the Euclidean distance. When local density is larger than the average, that is when

$$\delta(\mathbf{p}) > \frac{1}{|\mathcal{S}|} \sum_{\mathbf{q} \in \mathcal{S}} \delta(\mathbf{q}) \quad (5.1.5)$$

we know some properties about the region surrounding  $\mathbf{p}$ . For instance, if the point set is uniformly distributed then it is possible to find areas with a high-density in the case where there are two closely separated surfaces. In point sets of non-uniform distribution, high densities are found when the surface presents a joint discontinuity. The algorithm developed by Teichmann and Capps is structured as follow. After computing density information for each point they make a triangulation of the point set. Then they calculate the average density  $\delta(t)$  for each triangle  $\Delta_{abc}$  defined as:

$$\delta(t) = \frac{\delta(a) + \delta(b) + \delta(c)}{3\mu}, \quad (5.1.6) \quad \boxed{\text{delta\_t}}$$

where  $\mu$  is the global average density of the entire point set  $\mathcal{S}$ . If  $\delta(t)$  is greater than 1 the density of the point cloud is higher. Hence is necessary to define another value of  $\alpha$ :

$$\alpha' = \frac{\alpha}{\delta(t)^\sigma} \quad (5.1.7)$$

where  $\sigma$  is a value that is adjusted by the user. If  $\delta$  is less than 1 the  $\alpha$ -value is not modified. In this way it is possible to have a finer precision on the shape formed by the point set where the density is higher than the average density. Hence it is possible to distinguish two separated objects with different density.

## **5.2 The two-faceted cup**

## **5.3 Results for a TIR collimator**

## **5.4 The triangulation refinement approach**

## **5.5 The two-faceted cup**

## **5.6 Results for a Parabolic reflector**

## **5.7 Results for the Compound Parabolic Concentrator**

## **5.8 Results for a TIR collimator**

# **Chapter 6**

## **The inverse ray mapping method: analytic approach**

### **6.1 Explanation of the method**

[2]

### **6.2 Results for the two-faceted cup**

### **6.3 Results for the multi-faceted cup**

### **6.4 Discussions**



## Chapter 7

# The extended ray mapping method

- 7.1 Explanation of the method
- 7.2 Bisection procedure
- 7.3 Results for a parabolic reflector
- 7.4 Results for two different kind of TIR-collimators



## Chapter 8

# Extended method to systems with Fresnel reflection



## **Chapter 9**

# **Conclusions and remarks**



# Summary

I have changed the summary



# Curriculum Vitae



# Acknowledgments



# Bibliography

- mer1994three [1] H. Edelsbrunner and E. P. Mücke. Three-dimensional alpha shapes. *ACM Transactions on Graphics (TOG)*, 13(1):43–72, 1994.
- s2005Handbook [2] H. Gross. *Handbook of the Optical Systems*, volume 1. Wiley-VCH, 2005.
- echt1998hecht [3] E. Hecht. *Optics*. Parson Addison-Wesley, 2002.
- egies2013fast [4] J. Portegies and P. Lighting. Fast ray tracing in phase space for optical design. 2013.
- Ries:2 [5] H. Ries and A. Rabl. Edge-ray principle of nonimaging optics. *JOSA A*, 11(10):2627–2632, 1994.
- nn1998surface [6] M. Teichmann and M. Capps. Surface reconstruction with anisotropic density-scaled alpha shapes. In *Visualization'98. Proceedings*, pages 67–72. IEEE, 1998.
- Ting:1 [7] D. Z. Ting and T. C. McGill Jr. Monte Carlo simulation of light-emitting diode light-extraction characteristics. *Optical Engineering*, 34(12):3545–3553, 1995.

